Nano-imaging of intersubband transitions in van der Waals quantum wells

Schmidt, Peter; Vialla, Fabien; Latini, Simone; Massicotte, Mathieu; Tielrooij, Klaas-Jan; Mastel, Stefan; Navickaite, Gabriele; Danovich, Mark; Ruiz-Tijerina, David A.; Yelgel, Celal

Total number of authors:
14

Published in:
Nature Nanotechnology

Link to article, DOI:
10.1038/s41565-018-0233-9

Publication date:
2018

Document Version
Peer reviewed version

Nano-imaging of intersubband transitions in van der Waals quantum wells

Peter Schmidt[1], Fabien Vialla[1,2], Simone Latini[3,4], Mark Danovich[5], David A. Ruiz-Tijerina[5], Mathieu Massicotte[1], Klaas-Jan Tielrooij[1], Stefan Mastel[6], Gabriele Navickaite[1], Rainer Hillenbrand[6,7], Vladimir Falko[5], Kristian Thygesen[3], Frank Koppens[1,8]

[1]ICFO - Institut de Ciéncies Fotóniques, The Barcelona Institute of Science and Technology, 08860 Castelldefels (Barcelona), Spain
[2]Institut Lumière Matière UMR5306, Université Claude Bernard Lyon1 – CNRS, 69622 Villeurbanne Cedex, France
[3]Center for Atomic-scale Materials Design, Technical University of Denmark, DK-2800 Kongens Lyngby, Denmark
[4]Max Planck Institute for the Structure and Dynamics of Matter, 22761 Hamburg, Germany
[5]National Graphene Institute, University of Manchester, Manchester M13 9PL, United Kingdom
[6]CIC nanoGUNE Consolider, 20018 Donostia-San Sebastián, Spain
[7]IKERBASQUE, Basque Foundation for Science, 48011 Bilbao, Spain
[8]ICREA-Institució Catalana de Recerca i Estudis Avançats, 08010 Barcelona, Spain

Electronic and optoelectronic innovations have been driven for decades by progress in the growth of semiconducting heterostructures. Many applications in the infrared and terahertz range exploit intersubband transitions between quantized states in semiconductor quantum wells. However, current quantum well devices are limited in functionality and versatility by diffusive interfaces and the requirement of lattice-matched growth conditions. Two-dimensional (2D) materials hold unexplored potential to overcome these limitations, as they naturally form 'naked' quantum wells – van der Waals quantum wells – and can easily be combined into heterostructures with atomically sharp interfaces. Here, we introduce the concept of intersubband transitions in van der Waals quantum wells and report their first observation. By employing near-field local probing we spectrally resolve and electrostatically control the intersubband absorption with unprecedented spatial resolution. This work enables exploiting intersubband transitions with unknown design freedom and individual electronic and optical control suitable for photodetectors, LEDs and lasers.

Nanoscale confinement of charge carriers gives rise to a rich variety of physical phenomena that are not present in bulk materials, and lies at the heart of many modern optoelectronic applications [1-4]. One striking feature is that confinement leads to quantized energy levels, whose energy spacing increases with spatial confinement. Charge carriers can be confined in three dimensions (0D quantum dots [5]), in two dimensions (1D quantum wires [6]) or in one dimension (2D quantum wells). The latter is arguably the most well-known example and has led to the development of quantum well infrared photodetectors [7] and quantum cascade lasers (QCLs) [8] for mid infrared (MIR) to THz wavelengths. These devices rely on transitions of electrons (or holes) between the quantized states – intersubband transitions [9-11] – of a semiconductor quantum well (QW). In contrast to interband transitions, these intraband transitions exhibit very large oscillator strengths close to unity [9]. Currently, state-of-the-art quantum wells are typically grown by molecular beam epitaxy (MBE) of different III-V semiconductor alloys. This technology suffers from fundamental material limitations: Strict lattice matching conditions limit the available material combinations and the thermal growth causes atomic diffusion and increases interface roughness, restricting the performances of actual devices [12].

Recently, a new family of atomically thin materials has emerged as a promising platform for optoelectronic applications: 2D layered materials [13-17]. Studies of the optical properties of these semiconducting 2D materials have demonstrated unique features in the visible and near-infrared wavelength regions [18-21], all of which arise from interband electronic transitions. However, few-layer 2D materials also form natural QWs – van der Waals QWs – where charge carriers are confined to the nanoscale in one dimension and it is therefore natural to expect intersubband transitions to occur. In contrast to conventional QWs, van der Waals QWs provide defect free and atomically sharp interfaces, enabling the formation of ideal QWs, free of diffusive inhomogeneities. Furthermore, van der Waals QWs do not require epitaxial growth on a matching substrate and can therefore be easily isolated and coupled to other electronic systems such as Si CMOS or optical systems such as cavities and waveguides. QWs in 2D materials therefore hold the potential to overcome the two main limitations of their epitaxial counterparts. Additionally, any selection of 2D materials can be combined by stacking them into so-called van der Waals heterostructures, where van der Waals forces (rather than chemical bonds) hold the different layers together [14, 22].

Here, we introduce the concept of intersubband transitions in van der Waals quantum wells, report their first experimental observation, and provide detailed theoretical calculations. We probe the transitions between the quantized states within both the valence and the conduction band by investigating the MIR optical response of doped semiconducting transition metal dichalcogenides (TMDs). The TMDs were exfoliated on a Si/HfO_2 substrate - specifically chosen to avoid contributions from substrate phonons - and electron or hole doping was induced by applying a gate voltage between Si and TMD. Each investigated flake comprised several terraces of different layer number N, where charge carriers are quantum confined in the out-of-plane direction within the TMD flake, as illustrated in Figure 1a. As the QWs are not buried inside any material, we can perform scattering scanning near-field optical microscopy (s-SNOM), an innovative measurement approach allowing for spectral absorption measurements with a spatial resolution below 20 nm. We spectrally resolve intersubband resonances for the different QW thicknesses within a single TMD flake by varying the illumination photon energy, as schematically depicted in Figure 1b. Furthermore, we demonstrate in-situ control of the intersubband absorption strength by electrostatically tuning the charge carrier density of the TMD flake. Finally, to show the versatility of intersubband

transitions in 2D materials, we demonstrate intersubband absorption in both valence and conduction bands within a single device.

First, we lay the theoretical framework for intersubband transitions in van der Waals QWs. Figure 1c shows the band structure of a 2H-WSe_2 crystal with layer number N = 5, obtained by using ab-initio density functional theory (DFT) calculations including spin-orbit (SO) coupling (see SI for more details). It reveals the splitting of the lowest conduction (highest valence) band into several subbands. In contrast to monolayer TMD crystals, where both band edges appear at the K-points of the Brillouin zone [23], few layer WSe_2 has the valence band edge at the Γ point, and the conduction band edge at the Λ points, which are located close to the middle of the Γ-K segments in the Brillouin zone [24, 25]. This change in the spectral characteristics is determined by a strong overlap between the Γ and Λ points wave functions in neighboring monolayers which also determines the z-axis (out-of-plane) effective mass and the k_z dispersion in the bulk layered crystal [25]. For the edge of the valence band, which appears at the 3D Γ point in 2H-WSe_2, we can approximate the dispersion of holes as $E \approx \frac{\hbar^2 k_z^2}{2m_z} + \frac{p_{xy}^2}{2m_{xy}}(1 + \zeta k_z^2)$, where $m_z \approx 1.08\, m_e$ and $m_{xy} = 0.7\, m_e$ are the out-of-plane and in-plane effective masses, $\hbar$ is the reduced Planck constant, p_{xy} is the in-plane crystal momentum and $\zeta \approx -5.45$ Å^2 is an anisotropic non-parabolicity factor (see SI for details).

The splitting of the bands represents the quantized states in the quantum well. The wave numbers for these standing waves in the z-direction are determined by the (Dirichlet-Neumann) boundary conditions of the wave functions at the top and bottom interfaces ($z = \pm Nd/2$), with the monolayer thickness d. Figures 1d and 1e show these (Λ and Γ point) out-of-plane wave functions for electrons and holes, respectively, which represent a periodic modulation with the same periodicity as the atomic potential multiplied by an envelope function. The boundary conditions gives us$k_z = \pi j/(N + 2\nu)d$, with the subband index j and a phenomenological parameter ν to enforce the boundary condition (see SI for more details). The energy of the *j=1 → j=2* intersubband transition in a lightly p-doped film is then given by

$$E_{sub} = E_{j=2} - E_{j=1} \approx \frac{1}{(N+2\nu)^2}\frac{3\hbar^2\pi^2}{2m_z d^2}. \qquad (1)$$

This fits very well with the transition energies obtained from the DFT results, shown in Figures 1f and 1g for electrons and holes, respectively.

Now we turn to the experimental observation of intersubband transitions in van der Waals quantum wells. This is highly challenging using conventional far-field illumination [9, 26] since the lateral size of TMD flakes with constant thicknesses is smaller than the infrared diffraction limit, and intersubband transitions only couple to light with an out-of-plane polarization component. To overcome these challenges we used the s-SNOM and exploited the fact that exfoliated 2D materials naturally form a bare QW. The s-SNOM consists of a metalized atomic force microscope (AFM) tip that is illuminated by a continuous-wave (cw) laser source. The optical hot spot that is generated around the tip apex interacts in the near-field with the TMD flake underneath the tip. Importantly, the hot spot – of about 20 nm in diameter – contains out-of-plane polarization components and can therefore excite intersubband transitions inside the TMD flake. We collect the light scattered back by the tip, which carries information about the sample's complex permittivity and thus its absorption at the illumination photon energy E_{ph}. This allows us to spatially resolve intersubband transitions with an unprecedented resolution of 20 nm and a sensitivity high enough to detect the intersubband absorption of a single electron (on average) under the AFM tip. By combining interferometric and tip-modulated detection (Figure 2a), we record a complex optical signal s_3 at the third harmonic of the AFM tip oscillation frequency f_{tip}, whose absolute value $|s_3|$ increases monotonically with N (see SI), and whose phase φ_3 is – in the case of weak resonances – proportional to the optical absorption of the TMD flake (see SI). We use $|s_3|$ to identify N across the probed flake as shown in Figure 2b.

In order to isolate the absorption signal of intersubband transitions from background signal and noise sources like laser and interferometer drifts, we modulate the charge carrier density of WSe_2 by applying a square wave backgate voltage V_{BG} between 0 and -5 V between the Si wafer and two Cr/Au contacts evaporated on the TMD flake (Figure 2c, see SI). Applying V_{BG} modulates the doping of the WSe_2 flake between charge neutrality and p-doping, hence populating the first subband in the valence band and allowing hole intersubband transitions. When scanning over the same area of the flake as in Figure 2b, we simultaneously monitor V_{BG} and the gate-induced change in φ_3 - $\Delta\varphi_3$ - extracting the change of absorption of the WSe_2 flake induced by a change in carrier density. We note that this gate modulation technique improves the signal/noise ratio,

but the generally observed trends presented in this work are also visible without modulation technique (see SI).

A spatial map of $\Delta\varphi_3$ for E_{ph} = 117 meV over an area of 13x10 µm^2 with a spatial resolution of ~20 nm is shown in Figure 2d. A clearly enhanced absorption is observed in the area of the flake where N = 1 and N = 5. When repeating the same scan at E_{ph} = 165 meV, we only observe absorption in the area where N = 4 (Figure 2e). This distinct behavior originates from two different absorption contributions. i) We attribute the enhanced absorption of the N = 4 and N = 5 regions of the flake to intersubband transitions. Comparing the observed absorption energies with the ab-initio calculations from Figure 1g, we find that hole intersubband transitions occur at energies close to 165 and 117 meV for WSe_2 flakes with N = 4 and N = 5, respectively. Therefore, these spatial absorption maps are a first indication that we observe intersubband transitions. ii) The absorption in the monolayer region at E_{ph} = 117 meV corresponds to Drude absorption: Since the charge carriers induced by the applied V_{BG} are confined within a single atomic layer, the absorption due to free charge carriers is much higher than in the few-layer regions, where the same number of charge carriers is distributed over several layers (see SI). Thus the relative contribution of Drude absorption is larger in the monolayer region.

To corroborate this interpretation, we spectrally resolve the intersubband resonances by changing E_{ph} in small steps. We average the recorded optical signals s_3 over the areas of the flake with a constant thickness. Due to the interferometric detection, s_3 is a complex signal and allows us to recover both the real and imaginary part of the relative permittivity of WSe_2, ε_{WSe2}, by using a thin-film inversion model (see SI) [27, 28]. We note that the flake thickness, the effect of the substrate, as well as different measurement parameters like tapping amplitude and demodulation order are accounted for by our model, but the qualitative resonance features are directly visible in the raw data. Figure 3a shows both $\Delta\varphi_3$ and the obtained $Im(\varepsilon_{WSe2})$ when the WSe_2 flake is p-doped, assuming $Im(\varepsilon_{WSe2})$ = 0 for charge-neutral WSe_2 in the infrared frequency range. First, we identify a general decrease of $Im(\varepsilon_{WSe2})$ with E_{ph} for all layer thicknesses. We attribute this behavior to Drude absorption of holes that we account for (see SI) by a standard complex Drude term $\varepsilon_{\mathrm{Drude}}(\omega) = -\frac{D}{\omega\varepsilon_0}\frac{1}{i\tau^{-1}+\omega}$, with the vacuum permittivity

ε_0, the Drude weight D, scattering time τ, and $E_{ph} = \hbar\omega$. In order to quantitatively address the intersubband absorption resonances, we subtract the Drude contribution from the obtained $Im(\varepsilon_{WSe2})$ (Figure 3b). We clearly distinguish an absorption peak for N = 4, as well as enhanced absorption for N = 5 at low photon energies. A Gaussian fit to the N = 4 data yields a center energy of 167.5 ± 1.5 meV and a full width half maximum Γ = 33 ± 4 meV. The obtained $Re(\varepsilon_{WSe2})$ shows a resonance behavior at the same energy, supporting our conclusion that we indeed observe a resonant absorption. The experimentally observed resonance energy (168 meV) is slightly higher than the theoretical prediction (145 meV), which may be due to many-body effects [29] and corrections due to interactions with the electron or hole plasma [30].

We proceed with discussing the linewidth of the intersubband transitions. Due to the atomically smooth surfaces of 2D materials, we expect that the linewidth of van der Waals quantum wells is not significantly broadened by interface roughness scattering, which is the dominant broadening mechanism in III-V semiconductor quantum wells [31, 32]. As a result, intersubband absorption linewidths in 2D materials at low temperatures can reach the phonon-limited linewidth, which we calculate to be on the order of 0.5 meV (see SI) and therefore much smaller than in epitaxial quantum wells [31]. At room temperature, we calculate a larger linewidth $\Gamma \approx 7$ meV, which originates from the differences in in-plane effective masses in the different subbands. The holes in the second subband are heavier than in the first subband, spreading the absorption for high temperatures or strongly doped films to $\Gamma \approx \left[1 - \frac{m_1}{m_2}\right] \log 2 \max\{\varepsilon_F, k_B T\}$, where m_1 and m_2 are the in-plane masses in the first and second subband respectively, ε_F is the Fermi energy, k_B Boltzmann's constant and T the temperature (see SI for more details). The measured linewidth of Γ = 33 meV is larger than these theoretical calculations, which we attribute to the occurrence of non-vertical transitions involving momentum transfer. In order to quantify this, we examine in more detail the hot spot around the AFM tip apex that excites intersubband transitions. The in-plane momenta contributing to the near-field coupling are given by a broad Bell shaped function (see SI) peaking at a k-vector that is inversely related to the tip curvature [33]. Due to this broad momentum distribution, a wide range of non-vertical transitions with finite momentum transfer and a distribution of transition energies contribute to the signal. This leads to a broadening and blue shift of the absorption line shape. The sharpest features around the AFM tip

apex determine the in-plane momentum distribution and are typically around 12 nm for the used AFM tips (see SI). Calculations for this tip radius yield Γ = 24 meV (Figure 3c), indicating that tip-induced broadening is indeed responsible for the experimentally observed linewidth.

Another key signature of intersubband transitions is the dependence of the absorption α on the carrier density n_{2D}. For an ideal, infinitely deep quantum well, assuming parallel subbands and T = 0 K, calculations yield $\alpha = n_{2D}\frac{e^2\hbar f_{12}}{c\varepsilon m^*\Gamma}$ [11], with the electron charge e, speed of light c, oscillator strength f_{12} = 0.96 for the transition from the first to the second subband, and ε the static out-of-plane permittivity. In order to experimentally study this dependence we vary n_{2D} by changing the modulation amplitude of the backgate voltage, $V_{BG,max}$, at E_{ph} = 165 meV, which corresponds to the center energy of the N = 4 intersubband resonance. The measured (Drude-corrected) $Im(\varepsilon_{WSe2})$ as a function of n_{2D} is shown in Figure 4a. We observe a monotonic increase of the absorption with n_{2D}. This is consistent with the idealized square well model, although we note that the exact function of the increase might be affected by possible contributions from many-body effects and non-parabolic bands. Experimentally, we find a maximum absorption of α_{exp} = 0.017 ± 0.002 % (see SI) for a hole density n_{2D} = 9x10^{11} cm^{-2} (extracted from capacitance measurements on a separate device), which is in reasonable agreement with the idealized model yielding α = 0.026% for a WSe_2 crystal with N = 4. We note that the absorption will be significantly enhanced with narrower linewidths, reaching values as high as α = 1.7% for the phonon-limited linewidth Γ ≈ 7 meV.

We further demonstrate the versatility of 2D materials by ambipolar electrical control of intersubband transitions in the valence and conduction bands. We tune the carrier density from the p-doped to the n-doped regime and observe intersubband transitions in both cases. Interestingly, at E_{ph} = 117 meV, these transitions occur for different layer thicknesses. As we have seen before, we observe hole intersubband transitions in the N = 5 area of the flake (Figure 4b). However, when the flake is n-doped, we observe enhanced absorption due to electron intersubband transitions in the N = 6 region of the flake (Figure 4c). This observation that the electron transitions for a given E_{ph} occur in a thicker part of the flake than the hole transitions is in excellent agreement with our theoretical ab-initio calculations (see Figures 1f-g). In order to reach n- and p-doping

without leakage through the underlying oxide we use the AFM tip to induce additional doping to the flake (see SI). We apply a constant potential V_{WSe2} to the WSe_2 flake, which locally induces charge carriers (holes for $V_{WSe2} > 0$ and electrons for $V_{WSe2} < 0$) due to the capacitive coupling between the flake and the grounded, metallic AFM tip. In addition to this 'tip doping' we further apply a DC backgate voltage V_{BG} that can either enhance the effect of the 'tip doping' or cancel it.

In conclusion, we reported the first experimental observation of intersubband transitions in few-layer WSe_2 crystals with spatial and spectral measurements supported by detailed ab-initio calculations. The obtained spatial resolution of 20 nm cannot be obtained by classical far-field measurements. Intersubband transitions are not unique to WSe_2; they can be found in any gapped 2D material (see SI for similar measurements on MoS_2). This study represents a first step into a vast unexplored field that holds a plethora of opportunities. Our study offers a first glimpse of the physics and technology enabled by van der Waals quantum wells, enabling applications such as infrared detectors, sources, and lasers with the potential for compact integration with Si CMOS. Particularly appealing is the possibility of combining various 2D material QWs to any of the wide variety of different 2D crystals – including semimetals, dielectrics, topological insulators [34, 35], superconductors [36], and ferromagnets [37, 38] – with any relative lattice alignment angle between different layers, giving rise to an unprecedented freedom in designing novel optoelectronic devices. Additionally, each layer inside a van der Waals heterostructure can individually be contacted electrically [39] allowing for in-situ tuning of resonances and interactions as well as facile carrier injection. This paves the way to new phenomena that are not accessible in any other material class.

Acknowledgements:

We greatly acknowledge discussions with Prof. Simon Wall about the experimental measurement technique. We also like to thank Dr. Alexander Govyadinov on discussions about the thin-film inversion model. P.S. acknowledges financial support by a scholarship from the 'la Caixa' Banking Foundation. F.V. acknowledges financial support from Marie-Curie International Fellowship COFUND and ICFOnest program. M.M. thanks

the Natural Sciences and Engineering Research Council of Canada (PGSD3-426325-2012). K.-J.T. acknowledges support from a Mineco Young Investigator Grant (FIS2014-59639-JIN). F.K. acknowledges financial support from the Government of Catalonia trough the SGR grant (2014-SGR-1535), and from the Spanish Ministry of Economy and Competitiveness, through the "Severo Ochoa" Programme for Centres of Excellence in R&D (SEV-2015-0522), support by Fundacio Cellex Barcelona, CERCA Programme / Generalitat de Catalunya and the Mineco grants Ramón y Cajal (RYC-2012-12281) and Plan Nacional (FIS2013-47161-P and FIS2014-59639-JIN). Furthermore, the research leading to these results has received funding from the European Union Seventh Framework Programme under grant agreement no.696656 Graphene Flagship and the ERC starting grant (307806, CarbonLight).

References:

[1] Kroemer, H. (2001). Nobel Lecture: Quasi-electric Fields and Band Offset: Teaching Electrons New Tricks. *Reviews of Modern Physics*, *73*(3), 783–793. http://doi.org/10.1103/RevModPhys.73.783

[2] Alferov, Z. I. (2001). Nobel lecture: The double heterostructure concept and its applications in physics, electronics, and technology. *Reviews of Modern Physics*, *73*(3), 767–782. http://doi.org/10.1103/RevModPhys.73.767

[3] Hayashi, I., Panish, M. B., Foy, P. W., & Sumski, S. (1970). Junction lasers which operate continuously at room temperature. *Applied Physics Letters*, *17*(3), 109–111. http://doi.org/10.1063/1.1653326

[4] Nakamura, S., Mukai, T., & Senoh, M. (1994). Candela-class high-brightness InGaN/AlGaN double-heterostructure blue-light-emitting diodes. *Applied Physics Letters*, *64*(13), 1687–1689. http://doi.org/10.1063/1.111832

[5] Bhattacharya, P., & Mi, Z. (2007). Quantum-dot optoelectronic devices. *Proceedings of the IEEE*, *95*(9), 1723–1740. doi:10.1109/JPROC.2007.900897

[6] Wang, J., Gudiksen, M. S., Duan, X., Cui, Y., & Lieber, C. M. (2001). Highly polarized photoluminescence and photodetection from single indium phosphide nanowires. *Science*, *293*(5534), 1455–1457. doi:10.1126/science.1062340

[7] Levine, B. F. (1993). Quantum-well infrared photodetectors. *Journal of Applied Physics*, *74*(8), R1–R81. http://doi.org/10.1063/1.354252

[8] Faist, J., Capasso, F., Sivco, D., Sirtori, C., Hutchinson, A. L., & Cho, A. Y. (1994). Quantum cascade laser. *Science (New York, N.Y.)*, *264*(5158), 553–556. http://doi.org/10.1126/science.264.5158.553

[9] West, L. C., & Eglash, S. J. (1985). First observation of an extremely large-dipole infrared transition within the conduction band of a GaAs quantum well. Applied Physics Letters, 46(12), 1156. http://doi.org/10.1063/1.95742

[10] Helm, M. (2004). Intersubband semiconductor light sources: History, status, and future. *Infrared and Millimeter Waves, Conference Digest of the 2004 Joint 29th International Conference on 2004 and 12th International Conference on Terahertz Electronics, 2004.*, *2*, 57–58. http://doi.org/10.1109/ICIMW.2004.1421951

[11] Liu, H. C., & Capasso, F. (2000). Intersubband transitions in quantum wells: Physics and device applications I. In *Semiconductors and Semimetals* (Vol. 62, p. 323). http://doi.org/10.1016/B978-0-444-81769-3.50024-3

[12] Warwick, C. A., Jan, W. Y., Ourmazd, A., & Harris, T. D. (1990). Does luminescence show semiconductor interfaces to be atomically smooth? *Applied Physics Letters*, *56*(26), 2666–2668. doi:10.1063/1.102825

[13] Novoselov, K. S., Jiang, D., Schedin, F., Booth, T. J., Khotkevich, V. V, Morozov, S. V, & Geim, a K. (2005). Two-dimensional atomic crystals. *Proceedings of the National Academy of Sciences of the United States of America*, *102*(30), 10451–10453. doi:10.1073/pnas.0502848102

[14] Novoselov, K. S., Mishchenko, A., Carvalho, A., & Castro Neto, A. H. (2016). 2D materials and van der Waals heterostructures. *Science*. doi:10.1126/science.aac9439

[15] Mak, K. F., & Shan, J. (2016). Photonics and optoelectronics of 2D semiconductor transition metal dichalcogenides. *Nature Photonics*, *10*(4), 216–226. http://doi.org/10.1038/nphoton.2015.282

[16] Wang, Q. H., Kalantar-Zadeh, K., Kis, A., Coleman, J. N., & Strano, M. S. (2012). Electronics and optoelectronics of two-dimensional transition metal dichalcogenides. *Nature Nanotechnology*, *7*(11), 699–712. http://doi.org/10.1038/nnano.2012.193

[17] Koppens, F. H. L., Mueller, T., Avouris, P., Ferrari, A. C., Vitiello, M. S., & Polini, M. (2014). Photodetectors based on graphene, other two-dimensional materials and hybrid systems. *Nature Nanotechnology*, *9*(10), 780–793. http://doi.org/10.1038/nnano.2014.215

[18] Mak, K. F., Lee, C., Hone, J., Shan, J., & Heinz, T. F. (2010). Atomically thin MoS2: A new direct-gap semiconductor. *Physical Review Letters*, *105*(13), 136805. http://doi.org/10.1103/PhysRevLett.105.136805

[19] Ugeda, M. M., Bradley, A. J., Shi, S.-F., da Jornada, F. H., Zhang, Y., Qiu, D. Y., … Crommie, M. F. (2014). Giant bandgap renormalization and excitonic effects in a monolayer transition metal dichalcogenide semiconductor. *Nature Materials*, *13*(12), 1091–1095. http://doi.org/10.1038/nmat4061

[20] Schaibley, J. R., Yu, H., Clark, G., Rivera, P., Ross, J. S., Seyler, K. L., … Xu, X. (2016). Valleytronics in 2D materials. *Nature Reviews Materials*, *1*(11), 1–15. http://doi.org/10.1038/natrevmats.2016.55

[21] Mak, K. F., McGill, K. L., Park, J., & McEuen, P. L. (2014). The valley Hall effect in MoS2 transistors. *Science (New York, N.Y.)*, *344*(6191), 1489–92. http://doi.org/10.1126/science.1250140

[22] Geim, A. K., & Grigorieva, I. . V. (2013). Van der Waals heterostructures. *Nature*, *499*(7459), 419–25. http://doi.org/10.1038/nature12385

[23] Kormányos, A., Burkard, G., Gmitra, M., Fabian, J., Zólyomi, V., Drummond, N. D., & Fal'ko, V. (2014). k.p theory for two-dimensional transition metal dichalcogenide semiconductors. *2D Mater.*, *2*(2), 22001. http://doi.org/10.1088/2053-1583/2/2/022001

[24] Sahin, H., Tongay, S., Horzum, S., Fan, W., Zhou, J., Li, J., … Peeters, F. M. (2013). Anomalous Raman spectra and thickness-dependent electronic properties of WSe2. *Physical Review B*, *87*(16), 1–6. http://doi.org/10.1103/PhysRevB.87.165409

[25] Huang, W., Luo, X., Gan, C. K., Quek, S. Y., & Liang, G. (2014). Theoretical study of thermoelectric properties of few-layer MoS2 and WSe2. *Physical Chemistry Chemical Physics*, *16*(22), 10866. http://doi.org/10.1039/c4cp00487f

[26] Kane, M. J., Emeny, M. T., Apsley, N., Whitehouse, C. R., & Lee, D. (1988). Inter-sub-band absorption in GaAs/AlGaAs single quantum wells. *Semiconductor Science and Technology*, *3*, 722–725. http://doi.org/10.1088/0268-1242/3/7/015

[27] Govyadinov, A. a., Amenabar, I., Huth, F., Carney, P. S., & Hillenbrand, R. (2013). Quantitative Measurement of Local Infrared Absorption and Dielectric Function with Tip-Enhanced Near-Field Microscopy. *The Journal of Physical Chemistry Letters*, *4*(9), 1526–1531. http://doi.org/10.1021/jz400453r

[28] Govyadinov, A. A., Mastel, S., Golmar, F., Chuvilin, A., Carney, P. S., & Hillenbrand, R. (2014). Recovery of permittivity and depth from near-field data as a step toward infrared nanotomography. *ACS Nano*, *8*(7), 6911–6921. http://doi.org/10.1021/nn5016314

[29] Manasreh, M. O., Szmulowicz, F., Vaughan, T., Evans, K. R., Stutz, C. E., & Fischer, D. W. (1991). Origin of the Blueshift in the Intersubband Infrared Absorption in GaAs/Alo.3Ga0.7As Multiple Quantum Well. Physical Review B, 43(12), 9996–9999.

[30] Allen, S. J., Tsui, D. C., & B, V. (1993). On the absorption of infraredradiation by electrons in semiconductorinversionlayers. *Solid State Communications*, *88*(11), 939.

[31] Unuma, T., Yoshita, M., Noda, T., Sakaki, H., & Akiyama, H. (2003). Intersubband absorption linewidth in GaAs quantum wells due to scattering by interface roughness, phonons, alloy disorder, and impurities. *Journal of Applied Physics*, *93*(3), 1586–1597. http://doi.org/10.1063/1.1535733

[32] Tsujino, S., Borak, A., Müller, E., Scheinert, M., Falub, C. V., Sigg, H., … Faist, J. (2005). Interface-roughness-induced broadening of intersubband electroluminescence in

p-SiGe and n-GaInAs/AlInAs quantum-cascade structures. *Applied Physics Letters*, *86*(6), 1–3. http://doi.org/10.1063/1.1862344

[33] Fei, Z., Andreev, G. O., Bao, W., Zhang, L. M., S. McLeod, A., Wang, C., … Basov, D. N. (2011). Infrared nanoscopy of dirac plasmons at the graphene-SiO2 interface. *Nano Letters*, *11*(11), 4701–4705. doi:10.1021/nl202362d

[34] Fei, Z., Palomaki, T., Wu, S., Zhao, W., Cai, X., Sun, B., … Cobden, D. H. (2017). Edge conduction in monolayer WTe2. *Nature Physics*, *13*(7), 677–682. doi:10.1038/nphys4091

[35] Wu, S., Fatemi, V., Gibson, Q. D., Watanabe, K., Taniguchi, T., Cava, R. J., & Jarillo-Herrero, P. (2018). Observation of the Quantum Spin Hall Effect up to 100 Kelvin in a Monolayer Crystal. *Science*, *359*(6371), 76–79. http://doi.org/10.1126/science.aan6003

[36] Xi, X., Wang, Z., Zhao, W., Park, J.-H., Law, K. T., Berger, H., … Mak, K. F. (2015). Ising pairing in superconducting NbSe2 atomic layers. *Nature Physics*, *12*(2), 139–143. http://doi.org/10.1038/nphys3538

[37] Huang, B., Clark, G., Navarro-Moratalla, E., Klein, D. R., Cheng, R., Seyler, K. L., … Xu, X. (2017). Layer-dependent ferromagnetism in a van der Waals crystal down to the monolayer limit. *Nature*, *546*(7657), 270–273. http://doi.org/10.1038/nature22391

[38] Gong, C., Li, L., Li, Z., Ji, H., Stern, A., Xia, Y., … Zhang, X. (2017). Discovery of intrinsic ferromagnetism in two-dimensional van der Waals crystals. *Nature*, *546*(7657), 265–269. doi:10.1038/nature22060

[39] Britnell, L., Gorbachev, R. V., Jalil, R., Belle, B. D., Schedin, F., Mishchenko, A., … Ponomarenko, L. A. (2012). Field-effect tunneling transistor based on vertical graphene heterostructures. *Science*, *335*(6071), 947–950. doi:10.1126/science.1218461

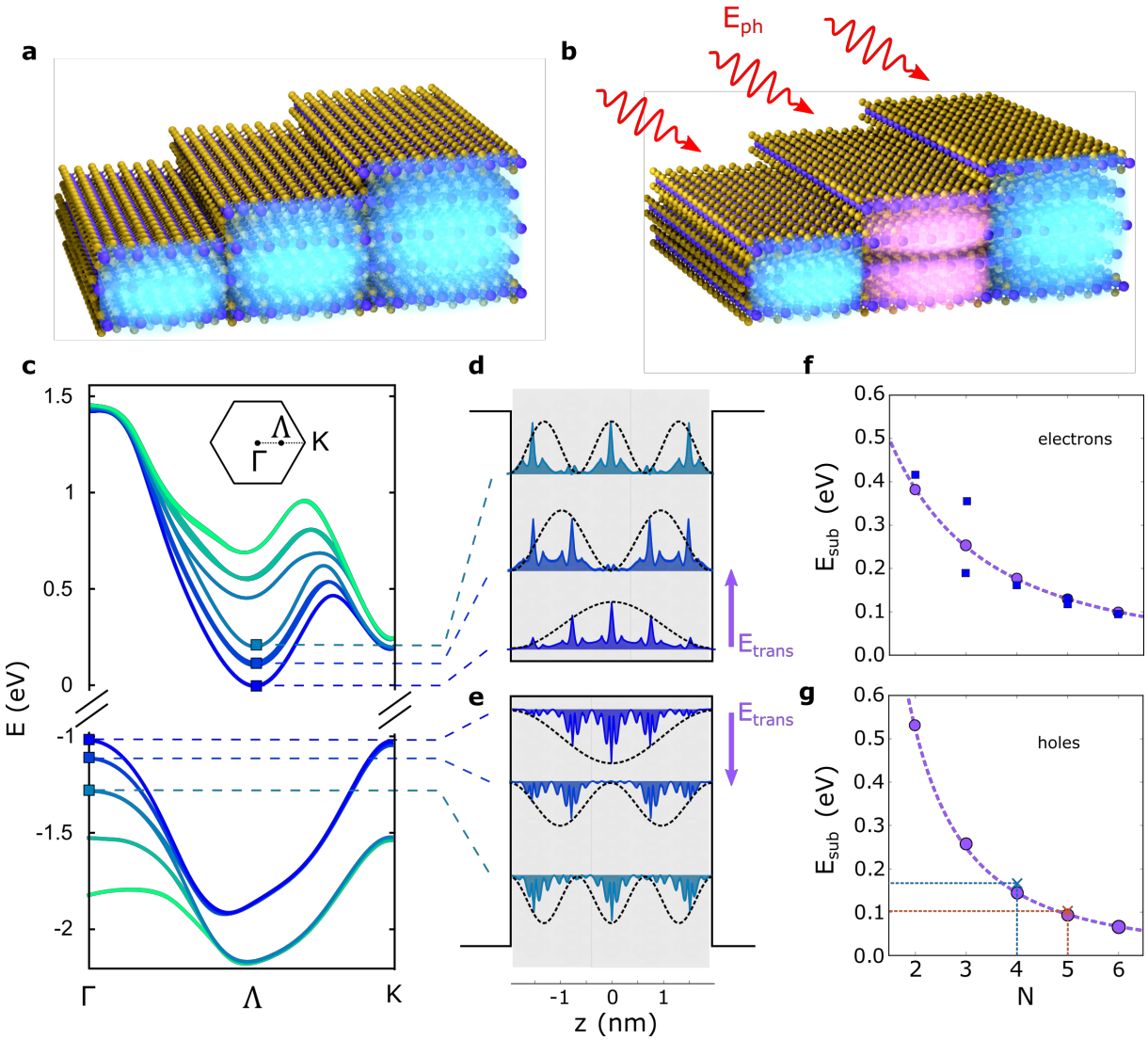

Figure 1 | Theoretical calculations on intersubband transitions in 2D materials. a, Schematic illustration of charge carriers (in blue) confined within a TMD flake consisting of different thicknesses. **b**, Upon light excitation with a photon energy E_{ph} and an out-of-plane polarization, charge carriers can be excited from the ground state to the first excited state (in pink), only if the intersubband transition energy for a given thickness is resonant with E_{ph}. **c**, Ab-initio DFT band structure calculations for a N = 5 2H-WSe_2 crystal. Shown are the five highest valence bands and the five lowest conduction bands, displayed along the Γ-K axis of the hexagonal Brillouin zone as indicated in the inset. SO coupling leads to an additional splitting of the bands around the Λ point. **d**, **e**, Calculated out-of-plane wave functions for a WSe_2 crystal with N = 5, at the points in the Brillouin zone as indicated in **c**: **d** shows the electron wave functions of the three lowest conduction bands at the Λ point, and **e** shows the hole wave functions of the three highest valence bands at the Γ point. Dashed lines represent the envelope functions assuming a perfect, infinitely deep square well potential. Solid black lines indicate the potential barrier experienced by the charge carriers. **f**, **g**, Calculated transition energies E_{sub} from the first to the second subband as indicated by the purple arrows in **d** and **e** as a function of N for electrons in the conduction band (**f**) and holes in the valence band (**g**). Purple circles represent the calculated transition energies neglecting SO coupling, while blue squares include SO coupling, which becomes important for N < 6. Dashed purple lines are fits of the modified infinite square well model (see main text) to the calculations without SO coupling yielding $\nu = 1.1$ for electrons (**f**) and $\nu = 0.09$ for holes (**g**).

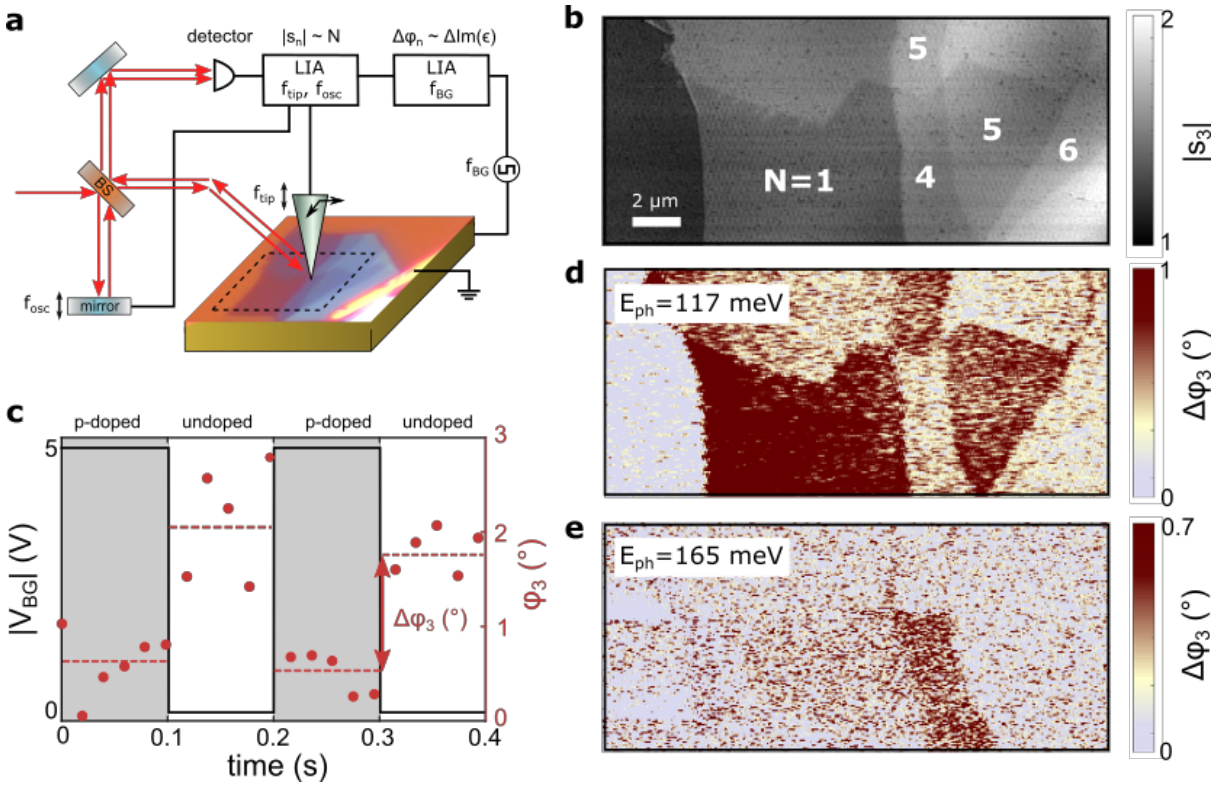

Figure 2 | Measurement setup and spatial absorption maps of a terraced WSe_2 flake. a, Real color microscope image of the WSe_2 flake and schematic illustration of the s-SNOM measurement setup. A MIR laser beam is divided into two paths by a beam splitter (BS) for interferometric detection: One path is reflected by a mirror oscillating with $f_{osc} \approx 300$ Hz, while the other beam is focused on the apex of a metalized AFM tip oscillating with $f_{tip} \approx 250$ kHz, where it interacts with the sample in the near-field. The back scattered light carries information about the sample permittivity at the illumination photon energy E_{ph}. Both beams are recombined and detected by a cooled HgCdTe (MCT) detector. In order to suppress the large background of light that is reflected from the AFM tip without interacting with the sample, the signal is evaluated at sidebands (arising due to the mirror oscillation with f_{osc}) of higher harmonics *n* of f_{tip} by a built-in lock-in amplifier (LIA). Due to the interferometric detection, the recorded signal s_n is complex and for our specific system of a thin WSe_2 flake on top of a thick substrate, $|s_n|$ increases monotonically with the number of layers N of the WSe_2 flake (see SI). s_n is further modulated by applying a square wave backgate voltage V_{BG} with frequency f_{BG} ($f_{BG} << f_{osc} << f_{tip}$) to the Si substrate thus modulating the doping of the WSe_2 flake. The change in phase of s_n with doping, $\Delta\varphi_n$, is proportional to the change in the imaginary part of the permittivity of WSe_2, $\Delta Im(\varepsilon_{WSe2})$. **b**, Spatial map of $|s_3|$ in arbitrary units obtained by scanning the AFM tip over the area of the flake marked by the dashed lines in (**a**). Different layer numbers can be identified by their optical signal and are indicated in the map. **c**, Backgate voltage $|V_{BG}|$ (black solid line, left axis) and corresponding phase of the third harmonic detector signal φ_3 (red dots, right axis) measured on the N = 1 area of the flake with $f_{BG} = 4.9$ Hz. Dashed red lines indicate the average of

φ_3 for when the flake is p-doped or charge neutral. The difference between these averages corresponds to $\Delta\varphi_3$. **d**, Spatial map of $\Delta\varphi_3$ obtained during the same scan as shown in (**b)** with E_{ph} = 117 meV. Higher values of $\Delta\varphi_3$ correspond to higher absorption. **e**, Spatial map of $\Delta\varphi_3$ obtained with E_{ph} = 165 meV scanning the same area of the flake as in **b** and **d**.

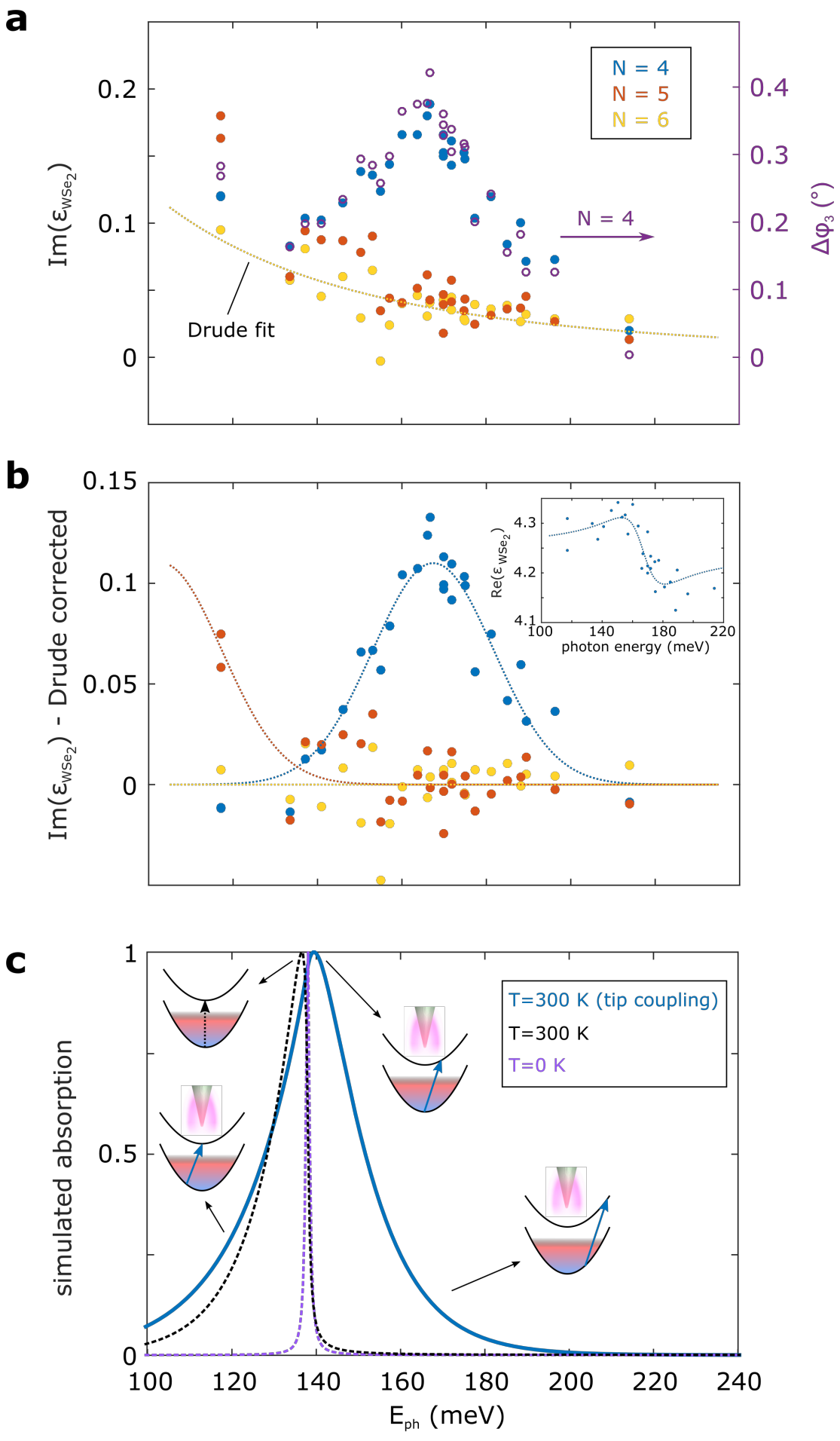
a
N = 4
N = 5
N = 6
N = 4
Drude fit
Im(ε_WSe2)
Δφ3 (°)
0.2
0.1
0
0.4
0.3
0.2
0.1
0
b
Im(ε_WSe2) - Drude corrected
0.15
0.1
0.05
0
Re(ε_WSe2)
4.3
4.2
4.1
100
140
180
220
photon energy (meV)
c
simulated absorption
1
0.5
0
T=300 K (tip coupling)
T=300 K
T=0 K
100
120
140
160
180
200
220
240
E_ph (meV)

Figure 3 | Intersubband absorption spectra in few-layer WSe_2. a, Imaginary part of ε_{WSe2} (filled dots) for different excitation photon energies E_{ph} and layer numbers N. $Im(\varepsilon_{WSe2})$ was calculated from the measured optical signals using a thin-film inversion model [27, 28]. The measurement was done at a hole concentration $n_{2D} \approx 9x10^{11}$ cm^{-2}. The yellow dashed line is a Drude fit to the N = 6 data. Also shown is the raw data $\Delta\varphi_3$ for N = 4 (open circles, right axis) **b**, Same data as in **(a)** with the Drude contribution subtracted. The blue dashed line shows a Gaussian fit to the N = 4 intersubband resonance, yielding a center energy of 167.5 ± 1.5 meV and linewidth Γ = 33 ± 4 meV. The orange dashed line is a Gaussian guide to the eye for the N = 5 intersubband resonance, assuming the same tip-induced Γ. Inset: $Re(\varepsilon_{WSe2})$ for the N = 4 area of the flake. The dashed line is a guide to the eye for a Lorentzian resonance. **c**, Absorption line shapes obtained from *ab-initio* calculations. Calculations were done for low carrier concentrations (Boltzmann distribution) at the Γ point of a p-doped 2H-WSe_2 crystal with N = 4 (see SI). The solid blue line shows the expected line shape for transitions excited by the near-field around an AFM tip with a radius of 12 nm at room temperature. The line shape is broadened and blue-shifted compared to far-field excitations with negligible in-plane momentum, shown as dashed lines for T = 300 K (black) and T ~ 0 K (purple). Insets illustrate the possible transitions from the first to the second subband.

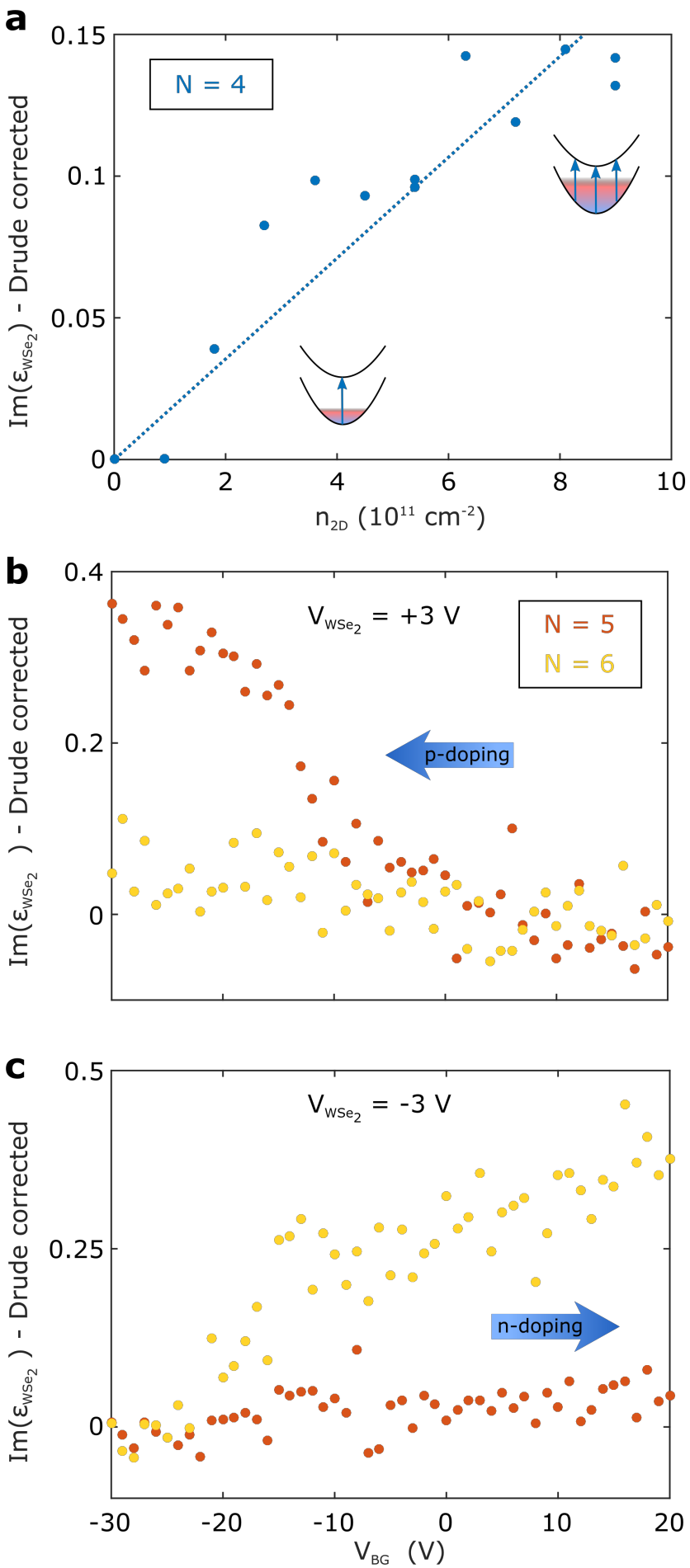
a
0.15
0.1
0.05
0
N = 4
Im(ε_WSe2) - Drude corrected
0
2
4
6
8
10
n_2D (10^11 cm^-2)
b
0.4
0.2
0
V_WSe2 = +3 V
N = 5
N = 6
p-doping
Im(ε_WSe2) - Drude corrected
c
0.5
0.25
0
V_WSe2 = -3 V
n-doping
-30
-20
-10
0
10
20
V_BG (V)

Figure 4 | Doping dependence of electron and hole intersubband absorption. a, Drude corrected $Im(\varepsilon_{WSe2})$ for different hole densities n_{2D}. The measurement was done at E_{ph} = 165 meV, which corresponds to the center of the N = 4 intersubband resonance. The carrier concentration was controlled by varying the maximum voltage $V_{BG,max}$ of the square wave function applied to the backgate. Insets show possible transitions for low and high carrier densities. **b, c,** Observation of hole (**b**, for N = 5 in orange) and electron (**c**, for N = 6 in yellow) intersubband transitions within the same WSe_2 flake at E_{ph} = 117 meV. Shown is the Drude corrected $Im(\varepsilon_{WSe2})$. The DC backgate voltage V_{BG} was increased stepwise from -30 to +20 V. The measurement was performed on a WSe_2 flake on top of a SiO_2 substrate. To reach higher doping levels, an additional DC voltage V_{WSe2} was applied to the WSe_2 flake, locally inducing holes (**b**, for V_{WSe2} = +3 V) or electrons (**c**, for V_{WSe2} = -3 V) due to interactions with the metallized, grounded AFM tip.